PNAS
www.pnas.org

Supplementary Information for

Optical signatures of multifold fermions in the chiral topological semimetal CoSi

B. Xu, et al.

Liang Wu.
E-mail: liangwu@sas.upenn.edu

This PDF file includes:

www.pnas.org/cgi/doi/10.1073/pnas.2010752117

Supporting Information Text

Appendix A: Reflectivity measurement, Kramers-Kronig analysis, Optical conductivity data on flux-grown sample and Hall resistivity data

The reflectivity $R(\omega)$ of CoSi was measured at a near-normal angle of incidence using a Bruker VERTEX 70v Fourier transform infrared spectrometer. An *in situ* gold overfilling technique (1) was used to obtain the absolute reflectivity. As shown in Figure S1(a), the reflectivity spectra have been measured over a very broad frequency range from 40 to 8 000 cm^{-1} on a shiny as-grown sample surface by using a series of combinations of sources, beamsplitters and detectors. The reflectivity spectra at different temperatures from 300 to 10 K were collected with an ARS-Helitran cryostat. Fig. S1(a) also shows the raw spectra measured for different frequency ranges at 10 and 300 K. It is evident that all spectra exhibit the same temperature dependence and are overlapping very well in the region where the spectra have been connected to perform the Kramers-Kronig analysis. This confirms the accuracy and reproducibility of the measured reflectivity spectra.

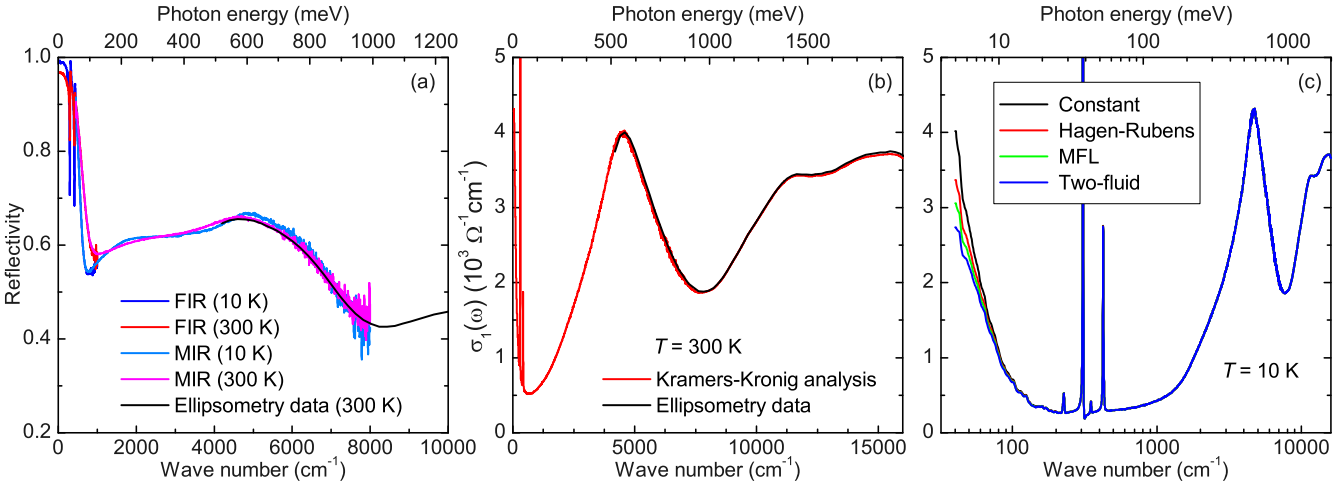

Fig. S1. (color online) (a) Reflectivity spectra $R(\omega)$ measured for different frequency ranges with a Fourier transform infrared reflectometer and with a grating-based spectroscopic ellipsometer. (b) Comparison of the optical conductivity spectrum at 300 K as obtained from the ellipsometry data and a Kramers-Kronig analysis of the reflectivity data. (c) The optical conductivity at 10 K obtained by the Kramers-Kronig analysis of $R(\omega)$ with different low-frequency extrapolations, such as Constant ($R(\omega) = \text{constant}$), Hagen-Rubens ($R(\omega) = 1 - A\sqrt{\omega}$), Marginal Fermi Liquid ($R(\omega) = 1 - A\omega$), and Two Fluid ($R(\omega) = 1 - A\omega^2$).

The optical conductivity $\sigma_1(\omega)$ was obtained from a Kramers-Kronig analysis of $R(\omega)$ (2). For the low-frequency extrapolation we used a Hagen-Rubens function $R = 1 - 2\sqrt{\frac{2\epsilon_0\omega}{\sigma_{DC}}}$, where σ_{DC} is the dc conductivity determined by the temperature-dependent DC four-terminal resistivity data. On the high-frequency side, the ellipsometry data were used, for which the spectrum in the near-infrared to ultraviolet range (4 000 – 50 000 cm^{-1}) was measured at room temperature with a commercial ellipsometer (Woollam VASE), and the Kramers-Kronig analysis was anchored by the room temperature ellipsometry data, as shown by the spectra in Fig. S1(b).

To verify the reliability of Kramers-Kronig analysis at low frequencies, in Fig. S1(c) we show how different low-frequency extrapolations during the Kramers-Kronig analysis of reflectivity influence the obtained spectra of optical conductivity. It shows that the uncertainty is very small, especially in the energy range above 20 meV where we studied the low-energy interband transitions associated with multifold fermions, since our reflectivity data have been measured with high accuracy down to very low energies of about 5 meV.

In Fig. S2, we show the optical conductivity data on the flux-grown CoSi (111) sample, measured under the same conditions as the CVT sample reported in the main text. Because of the cubic symmetry, the conductivity is the same on (001) and (111) facets. The temperature dependent real part of the conductivity is shown in Fig. S2(a). The results are very similar to the CVT sample. The 10 K curve also shows a kink around 0.2 eV. It also has a peak around 0.6 eV and sharp Drude and phonon peaks at low temperature. In Fig. S2 (b), we show the 10 K conductivity (blue) and the remainder after subtracting single sharp Drude (green) and four sharp phonon (gray) contributions. The remaining conductivity spectrum is shown in red and is also shown in Fig. 5 in the main text (black).

In Fig. S3, we show the typical Hall resistivity data on a CVT-grown and a flux-grown CoSi at 2 K. The linear negative Hall resistivity shows the dominating high-mobility electrons from the pocket at the R point. The carrier density is 2.1 $\times$ 10^{20} cm^{-3} and 2.8 $\times$ 10^{20} cm^{-3} for the CVT-grown and flux-grown samples, respectively. The mobility is $\approx$ 2,000 cm^2/Vs for the CVT sample while it is $\approx$ 6,700 cm^2/Vs for the flux-grown sample as one could see some quantum oscillations at high field in the latter sample. The residual resistivity ratio (RRR) for these two samples are 10 and 34 respectively. Note that these two samples are different from those measured by optical conductivity.

As shown in the inset of Fig. 4(a) of the main text, the RRR in the two samples measured by optical conductivity is $\sim$ 10, while it was 1.5 in previous studies (3, 4). While the room temperature resistivity is similar, the low-temperature value in our

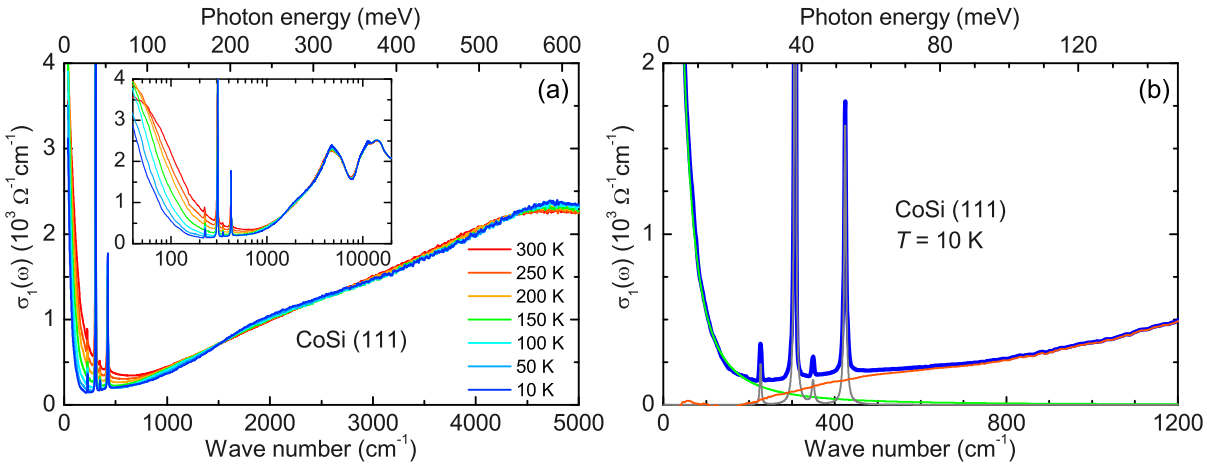

Fig. S2. (a) Temperature-dependent optical conductivity spectra $\sigma_1(\omega)$ of a flux-grown CoSi (111) sample. (b) Optical conductivity of CoSi at 10 K (blue); thin solid lines represent fit contributions of the Drude term (green) and phonon modes (grey), as well as the rest of the interband contributions to $\sigma_1(\omega)$ (red).

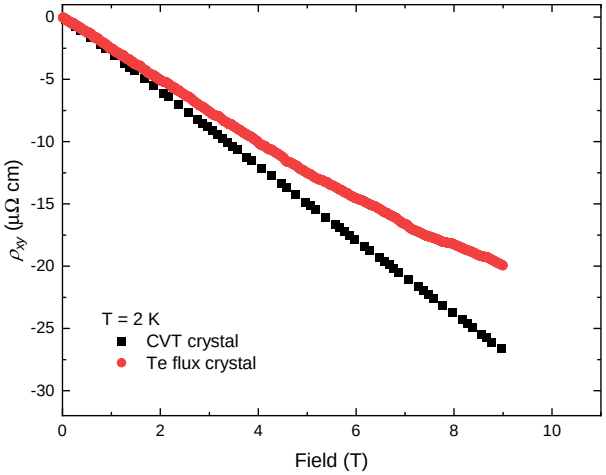

Fig. S3. Hall resistivity data on a CVT-grown and a flux-grown CoSi at 2 K.

sample is usually one order of magnitude smaller than previous ones (3, 4). We also observe much sharper phonon peaks in our crystal, which most likely indicates much better crystal quality in terms of lower carrier density and higher mobility. The onset of interband excitations in our samples is around 20 meV while it was 125 meV in previous studies (3, 4), which is consistent with lower chemical potential (Pauli-blocking energy) in our samples.

Appendix B: Optical conductivity formula

The complex optical conductivity $\sigma(\omega)$ is defined through

$$j^a(\omega) = \sigma^{ab}(\omega)E^b(\omega), \quad [1]$$

where the superscripts a and b represent Cartesian directions, $\mathbf{j}(\omega)$ is the Fourier component of $\mathbf{j}(t) = \sum_\omega \mathbf{j}(\omega)e^{-i\omega t}$, and $\mathbf{E}(\omega)$ is the Fourier component of $\mathbf{E}(t) = \sum_\omega \mathbf{E}(\omega)e^{-i\omega t}$. Using linear response theory, the complex optical conductivity is expressed as

$$\sigma^{ab}(\omega) = ie^2\hbar \sum_{m\neq n} \int \frac{d^3\mathbf{k}}{8\pi^3} \frac{f_{nm}}{E_{nm}} \frac{v^a_{nm}v^b_{mn}}{E_{nm} - \hbar\omega + i\eta}, \quad [2]$$

where $f_{nm}(\mathbf{k}) = f_n(\mathbf{k}) - f_m(\mathbf{k})$ is the Fermi-Dirac occupation difference between the n^{th} and m^{th} band at $\mathbf{k}$, $E_{nm}(\mathbf{k}) = E_n(\mathbf{k}) - E_m(\mathbf{k})$ is the band energy difference between these two bands, $v^a_{nm} = < n\mathbf{k}|v^a|m\mathbf{k} >$ is the velocity matrix element, and η accounts phenomenologically for disorder-related broadening.

The real part of the complex linear conductivity, which we refer to as the linear conductivity in this paper, is

$$\sigma^{ab}(\omega) = -\pi e^2\hbar \sum_{m\neq n} \int \frac{d^3\mathbf{k}}{8\pi^3} \frac{f_{nm}}{E_{nm}} v^a_{nm}v^b_{mn}\delta(E_{nm} - \hbar\omega). \quad [3]$$

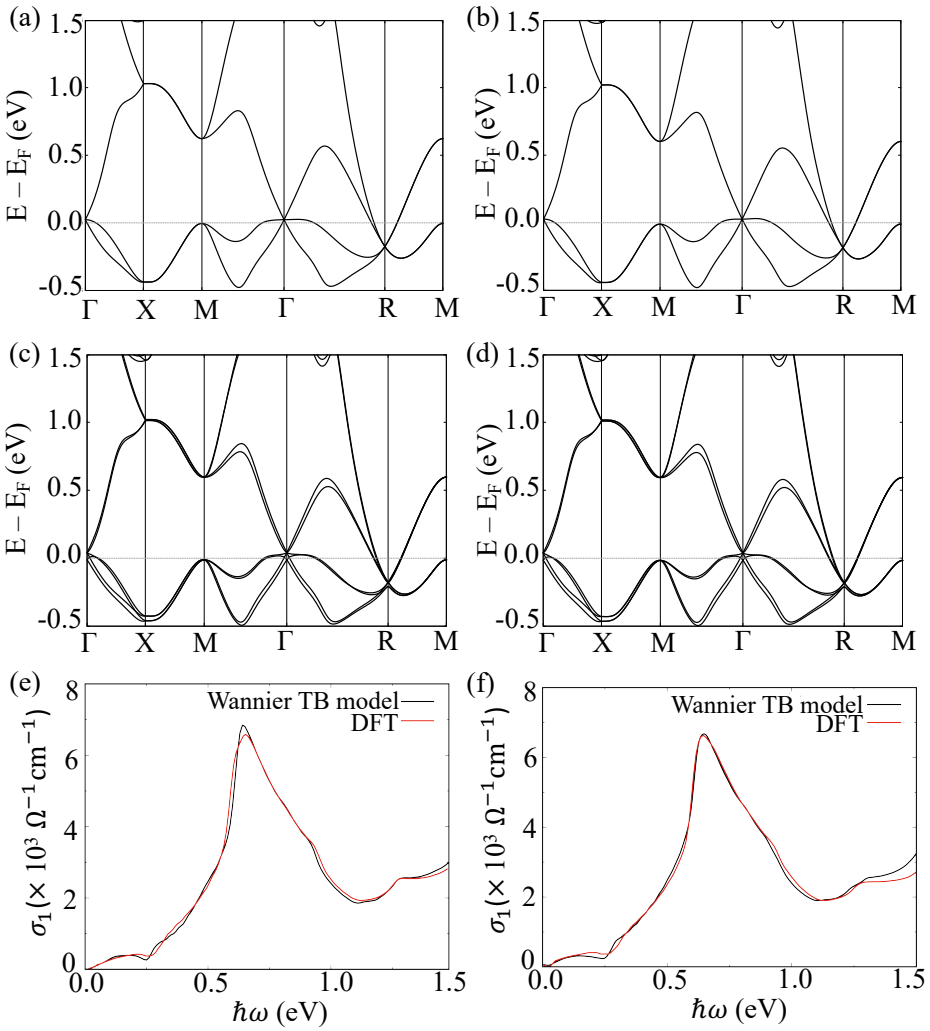

Fig. S4. (a) The band structure calculated from first-principles calculations without SOC; (b) The band structure calculated from the Wannier tight-binding model without SOC. (c) The band structure calculated from first-principles calculations with SOC. (d) The band structure calculated from Wannier tight-binding model with SOC. (e) Comparison between the conductivity calculated from first-principles calculations with non-SOC bands and that from Wannier tight-binding model; (f) Comparison between the conductivity calculated from first-principles calculations with SOC bands and that from the Wannier tight-binding model.

This expression is symmetric under exchange $m \leftrightarrow n$ if $a = b$. Given any positive $\hbar\omega$, the delta function will be nonzero only when $E_{nm} > 0$, or $n > m$, so the summation over bands where $m \neq n$ could be safely replaced by the summation where $n \in$ unocc and $m \in$ occ, where unocc and occ refer to unoccupied and occupied states respectively. The conductivity is also symmetric under the exchange $\omega \leftrightarrow -\omega$. Note that, when computing the optical conductivity from non-SOC bands, the conductivity should be multiplied by a factor of 2 to account for the spin degeneracy of the bands.

Appendix C: Computational details of first-principles calculations

We performed first-principles density functional theory (DFT) calculations in the software package of Quantum Espresso, with norm-conserving pseudopotentials generated from the OPIUM package. We chose the kinetic energy cutoff for th wavefunctions to be 90 Ry, and we used an $8 \times 8 \times 8$ k-point sampling grid for the crystal structure and band structure calculations. The relaxed lattice constants of CoSi are $a = 4.485$ Å.

Next, we used the software package Wannier90 to construct a tight-binding model in the basis of maximally-localized Wannier functions, fitted to the first-principles calculation results. To construct this model, we chose the initial projection functions to be s- and d-orbitals of Co, and s- and p-orbitals of Si; the converged maximally-localized Wannier functions that span the Bloch state valence manifold are well-localized in real space. The model can describe the electronic bands up to 1.5 eV above the Fermi level accurately, allowing us to calculate the conductivity accurately up to that energy scale. The comparison between the bands obtained from first-principles calculations and from this tight-binding model is shown in Fig. S4 (a-d). Here, we also calculated the conductivity with different smearing width shown in Fig. S5. As the smearing width increases, the dip around 0.25 eV get smeared out and the peak around 0.6 eV gets broadened.

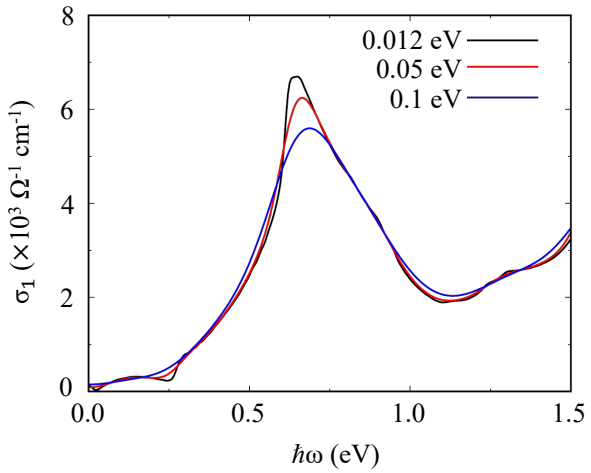

Fig. S5. The optical conductivity calculated from the Wannier TB model (w SOC) with different smearing width and the same number of $500 \times 500 \times 500$ k-points

We calculate the conductivity from DFT directly and from the solutions of the tight-binding model, and these are compared in Fig. S4 (e-f). In both calculations, to achieve faster convergence, the delta function $\delta(E_{nm} - \hbar\omega)$ in Eq. 3 is replaced by a broadened delta function $\tilde{\delta}(E_{nm} - \hbar\omega)$, expressed in the form of Gaussian function

$$G(E_{mn}, \hbar\omega, \sigma) = \frac{1}{\sqrt{\pi}\sigma} e^{-(\frac{E_{mn}-\hbar\omega}{\sigma})^2} \quad [4]$$

where σ, the width of the function, represents the carrier lifetime in materials. Since one of our primary goals is to focus on the slope of the linear conductivity at low frequency, which is controlled by the slope of the dispersing band of the spin-1 three-fold degenerate node at Γ, we choose carefully the size of the k-point sampling and the smearing width σ such that the Gaussian function can capture the energy change between adjacent k-points. In other words, we choose $\frac{dE}{dk} \approx \frac{\Delta E}{\Delta k}$, where $\frac{dE}{dk}$ is the slope of the dispersing bands around Γ, which, in our case, is 1.231 eV·Å, and Δk is the distance between adjacent k-points in a chosen k-point grid. For example, if we use a $150 \times 150 \times 150$ k-point grid to calculate the optical conductivity, the smearing width is chosen to be $\sigma = 12$ meV, which are used in Fig. S4 (e-f) for the DFT and Wannier tight-binding calculation. In the main text, we used $500 \times 500 \times 500$ k-point grid and $\sigma = 5$ meV for the Wannier tight-binding calculation. We also perform a calculation with a Gaussian broadening of 1.2 meV and 3 meV, and the latter is the experimental Drude peak width at 10 K, and the results with four different broadening (1.2 meV, 3 meV, 5 meV and 12 meV) overlaps with each other. Note that 3 meV is the low-temperature Drude peak width in both samples, which is a reasonable estimate of the broadening.

The calculations of the velocity matrix elements in Quantum Espresso is implemented through $v^a_{nm} = p^a_{nm}/m_0$, where m_0 is the electron mass and p^a_{nm} is the momentum matrix element. For the tight-binding model from Wannier90, the velocity matrix elements are calculated from $< n\mathbf{k}|\mathbf{v}|m\mathbf{k} >= -\frac{i}{\hbar}(E_{m\mathbf{k}} - E_{n\mathbf{k}})\mathbf{A}_{nm}(\mathbf{k})$, where the Berry connection is $\mathbf{A}_{nm}(\mathbf{k}) =< n\mathbf{k}|i\nabla_{\mathbf{k}}|m\mathbf{k} >$.

Appendix D: Velocity matrix elements and momentum-resolved contribution

Along the $\Gamma - R - M$ lines, the contributions to the peak at 0.62 eV in the optical conductivity originate mainly from the $R - M$ line, as can be seen from the main text. This can be further analyzed by focusing on the velocity matrix elements (Fig. S6(a)) and momentum-resolved JDOS (Fig. S6(b)) individually. As can be seen from Fig. S6, the magnitude of the velocity matrix elements are comparable on both lines, but the JDOS is much larger on the $R - M$ line than on the $\Gamma - R$ line. This suggests that the energy difference between the bands along the $R - M$ line are much closer to 0.62 eV, which makes them contribute more to the peak at 0.62 eV in the conductivity.

Appendix E: Contributions of spin-orbit-split bands along the $R - M$ line

When turning on SOC, a peak at around 0.011 eV appears in the calculated optical conductivity, as shown in Fig. S7(a). This peak originates from the spin-orbit-split bands along the $R - M$ high-symmetry line, as can be seen in Fig. S7(b). Without SOC, these bands are degenerate in energy; since the pair of bands along the $R - M$ line crosses the Fermi level, transitions are enabled at k-points where one band is below the Fermi level and the other is above E_F. The transition energy, or the position of the peak, indicates the SOC strength of CoSi.

Note that when calculating the peak, the smearing width σ has to be much smaller than the photon energy step; otherwise the peak will lead to nonzero conductivity at $\hbar\omega = 0$ eV. In the main text and this section, we used the smearing width $\sigma = 0.0012$ eV and the energy step $\Delta(\hbar\omega) = 0.005$ eV, and correspondingly a very dense kpoint sampling scheme, in order to show the position of the peak. In Appendix G, we used the smearing width $\sigma = 0.012$ eV.

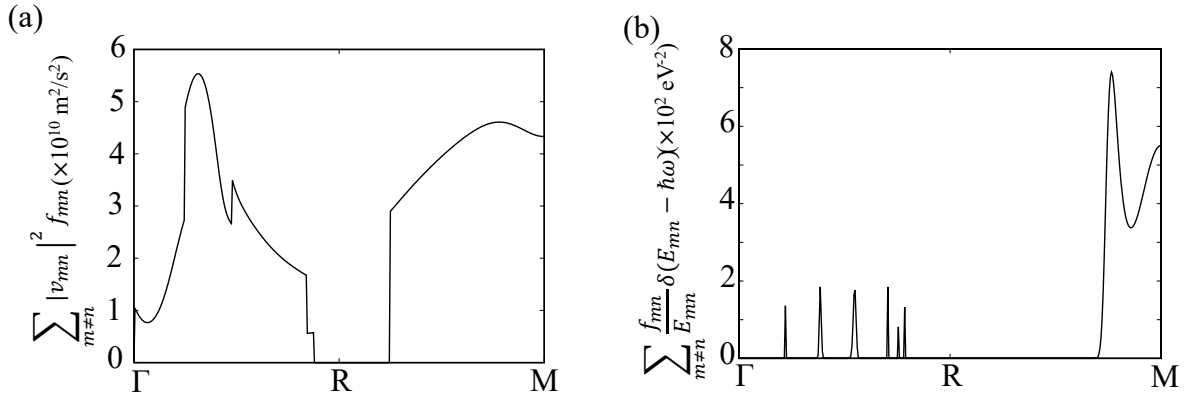

Fig. S6. (a) The sum of velocity matrix elements (including Fermi-Dirac occupation) $\sum_{nm} v^a_{nm}(\mathbf{k}) v^a_{mn}(\mathbf{k}) f_{nm}(\mathbf{k})$, and (b) the sum of delta function (including Fermi-Dirac occupation) $\sum_{nm} \delta(E_{mn}(\mathbf{k}) - \hbar\omega) \frac{f_{nm}(\mathbf{k})}{E_{nm}(\mathbf{k})}$.

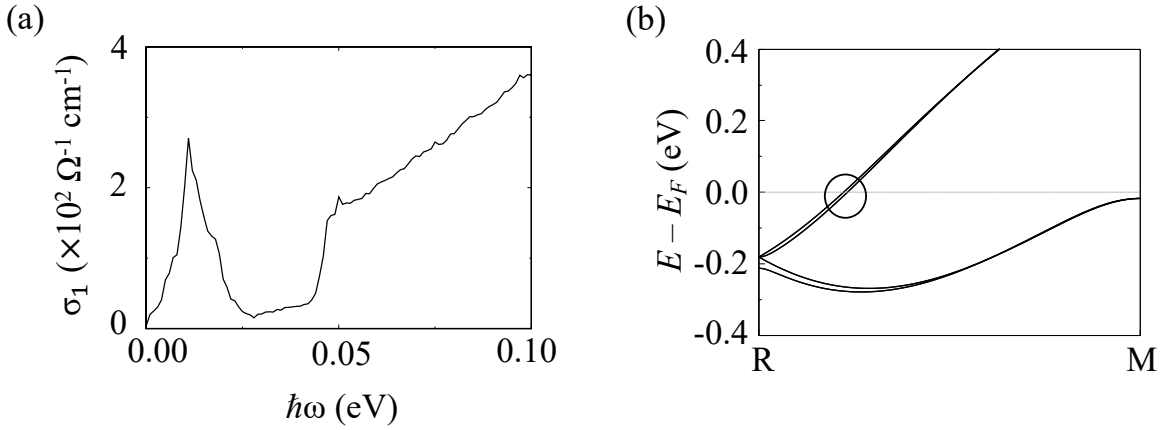

Fig. S7. (a) The calculated optical conductivity from SOC-split bands. (b) The calculated band structure (including SOC) along the $R - M$ high-symmetry line of CoSi.

Appendix F: Linear Models

The low-energy Hamiltonian without SOC, describing the spin-1 fermion node at Γ is

$$H = E_0 \hat{I}_{3\times 3} + \hbar v_F \begin{pmatrix} 0 & ik_x & -ik_y \\ -ik_x & 0 & ik_z \\ ik_y & -ik_z & 0 \end{pmatrix}, \quad [5]$$

where the parameter $E_0 = E_{\text{node}} - E_f = 0.0222$ eV is the energy difference between the node and Fermi energy, and $v_F = 1.231$ eV·Å is the Fermi velocity. The fitted band structures along $M - \Gamma - R$ high-symmetry lines are shown in Fig. S8 (a).

The low-energy Hamiltonian with SOC, describing the spin-$\frac{3}{2}$ and spin-$\frac{1}{2}$ node at Γ, is

$$H = E_0 \hat{I}_{6\times 6} + \epsilon \hat{\Delta} + \lambda_1 \mathbf{D}_1 \cdot \mathbf{k} + \lambda_2 \mathbf{D}_2 \cdot \mathbf{k} + \lambda_3 \mathbf{D}_3 \cdot \mathbf{k} + \lambda_4 \mathbf{D}_4 \cdot \mathbf{k} \quad [6]$$

where $\mathbf{D}_i \cdot \mathbf{k} = D_{ix}k_x + D_{iy}k_y + D_{iz}k_z$ (i = 1, 2, 3, 4), and

$$\hat{\Delta} = \begin{pmatrix} 1 & 0 & 0 & 0 & 0 & 0 \\ 0 & 1 & 0 & 0 & 0 & 0 \\ 0 & 0 & 1 & 0 & 0 & 0 \\ 0 & 0 & 0 & 1 & 0 & 0 \\ 0 & 0 & 0 & 0 & -2 & 0 \\ 0 & 0 & 0 & 0 & 0 & -2 \end{pmatrix},$$

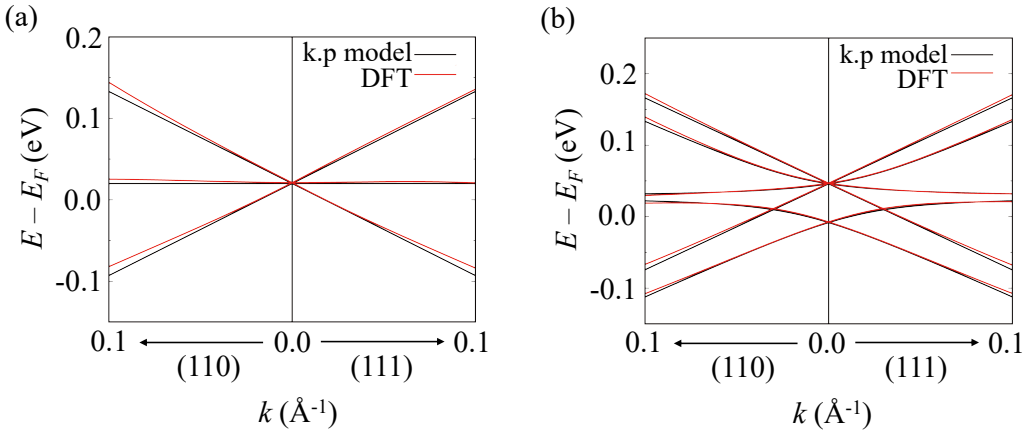

Fig. S8. The comparison between the CoSi band structures near Γ obtained from DFT (black) and from the $k \cdot p$ model (red) without SOC (a) and with SOC (b).

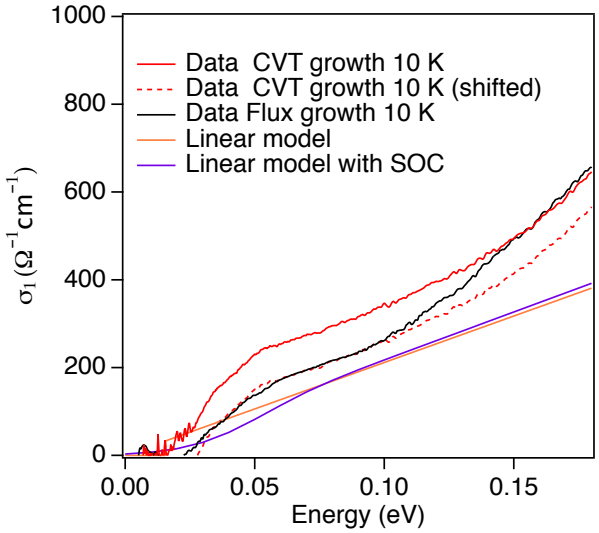

Fig. S9. Inter-band optical conductivity in CoSi from measurement in both CVT- and flux- grown samples (red and black curves) along with the linear model without and with spin-orbit coupling. The dashed red line has a down-shift of 80 $\Omega^{-1}cm^{-1}$ from the solid red curve.

$$D_{1x} = \begin{pmatrix} 0 & \frac{\sqrt{3}}{2} & 0 & 0 & -\frac{\sqrt{3}}{2\sqrt{2}} & 0 \\ \frac{\sqrt{3}}{2} & 0 & 1 & 0 & 0 & -\frac{1}{2\sqrt{2}} \\ 0 & 1 & 0 & \frac{\sqrt{3}}{2} & \frac{1}{2\sqrt{2}} & 0 \\ 0 & 0 & \frac{\sqrt{3}}{2} & 0 & 0 & \frac{\sqrt{3}}{2\sqrt{2}} \\ -\frac{\sqrt{3}}{2\sqrt{2}} & 0 & \frac{1}{2\sqrt{2}} & 0 & 0 & 1 \\ 0 & -\frac{1}{2\sqrt{2}} & 0 & \frac{\sqrt{3}}{2\sqrt{2}} & 1 & 0 \end{pmatrix},$$

$$D_{1y} = \begin{pmatrix} 0 & -\frac{\sqrt{3}i}{2} & 0 & 0 & \frac{\sqrt{3}i}{2\sqrt{2}} & 0 \\ \frac{\sqrt{3}i}{2} & 0 & -i & 0 & 0 & \frac{i}{2\sqrt{2}} \\ 0 & i & 0 & -\frac{\sqrt{3}i}{2} & \frac{i}{2\sqrt{2}} & 0 \\ 0 & 0 & \frac{\sqrt{3}i}{2} & 0 & 0 & \frac{\sqrt{3}i}{2\sqrt{2}} \\ -\frac{\sqrt{3}i}{2\sqrt{2}} & 0 & -\frac{i}{2\sqrt{2}} & 0 & 0 & -i \\ 0 & -\frac{i}{2\sqrt{2}} & 0 & -\frac{\sqrt{3}i}{2\sqrt{2}} & i & 0 \end{pmatrix},$$

$$D_{1z} = \begin{pmatrix} \frac{3}{2} & 0 & 0 & 0 & 0 & 0 \\ 0 & \frac{1}{2} & 0 & 0 & \frac{1}{\sqrt{2}} & 0 \\ 0 & 0 & -\frac{1}{2} & 0 & 0 & \frac{1}{\sqrt{2}} \\ 0 & 0 & 0 & -\frac{3}{2} & 0 & 0 \\ 0 & \frac{1}{\sqrt{2}} & 0 & 0 & 1 & 0 \\ 0 & 0 & \frac{1}{\sqrt{2}} & 0 & 0 & -1 \end{pmatrix},$$

$$D_{2x} = \begin{pmatrix} 0 & 0 & 0 & -\frac{3}{2} & 0 & 0 \\ 0 & 0 & -\frac{3}{2} & 0 & 0 & 0 \\ -\frac{3}{2} & 0 & 0 & 0 & 0 & 0 \\ -\frac{3}{2} & 0 & 0 & 0 & 0 & 0 \\ 0 & 0 & 0 & 0 & 0 & \frac{3}{2} \\ 0 & 0 & 0 & 0 & \frac{3}{2} & 0 \end{pmatrix},$$

$$D_{2y} = \begin{pmatrix} 0 & 0 & 0 & -\frac{3i}{2} & 0 & 0 \\ 0 & 0 & \frac{3i}{2} & 0 & 0 & 0 \\ 0 & -\frac{3i}{2} & 0 & 0 & 0 & 0 \\ \frac{3i}{2} & 0 & 0 & 0 & 0 & 0 \\ 0 & 0 & 0 & 0 & 0 & -\frac{3i}{2} \\ 0 & 0 & 0 & 0 & \frac{3i}{2} & 0 \end{pmatrix},$$

$$D_{2z} = \begin{pmatrix} -\frac{3}{2} & 0 & 0 & 0 & 0 & 0 \\ 0 & \frac{3}{2} & 0 & 0 & 0 & 0 \\ 0 & 0 & -\frac{3}{2} & 0 & 0 & 0 \\ 0 & 0 & 0 & \frac{3}{2} & 0 & 0 \\ 0 & 0 & 0 & 0 & \frac{3}{2} & 0 \\ 0 & 0 & 0 & 0 & 0 & -\frac{3}{2} \end{pmatrix},$$

$$D_{3x} = \begin{pmatrix} 0 & -\frac{\sqrt{3}}{2} & 0 & 0 & -\frac{\sqrt{3}}{\sqrt{2}} & 0 \\ -\frac{\sqrt{3}}{2} & 0 & 1 & 0 & 0 & \frac{1}{\sqrt{2}} \\ 0 & 1 & 0 & -\frac{\sqrt{3}}{2} & -\frac{1}{\sqrt{2}} & 0 \\ 0 & 0 & -\frac{\sqrt{3}}{2} & 0 & 0 & \frac{\sqrt{3}}{\sqrt{2}} \\ -\frac{\sqrt{3}}{\sqrt{2}} & 0 & -\frac{1}{\sqrt{2}} & 0 & 0 & -\frac{1}{2} \\ 0 & \frac{1}{\sqrt{2}} & 0 & \frac{\sqrt{3}}{\sqrt{2}} & -\frac{1}{2} & 0 \end{pmatrix},$$

$$D_{3y} = \begin{pmatrix} 0 & 0 & 0 & \frac{3i}{2} & 0 & 0 \\ 0 & 0 & \frac{i}{2} & 0 & 0 & i\sqrt{2} \\ 0 & -\frac{i}{2} & 0 & 0 & i\sqrt{2} & 0 \\ -\frac{3i}{2} & 0 & 0 & 0 & 0 & 0 \\ 0 & 0 & -i\sqrt{2} & 0 & 0 & \frac{i}{2} \\ 0 & -i\sqrt{2} & 0 & 0 & -\frac{i}{2} & 0 \end{pmatrix},$$

$$D_{3z} = \begin{pmatrix} 0 & 0 & \frac{\sqrt{3}}{2} & 0 & 0 & \frac{\sqrt{3}}{\sqrt{2}} \\ 0 & -1 & 0 & -\frac{\sqrt{3}}{2} & \frac{1}{\sqrt{2}} & 0 \\ \frac{\sqrt{3}}{2} & 0 & 1 & 0 & 0 & \frac{1}{\sqrt{2}} \\ 0 & -\frac{\sqrt{3}}{2} & 0 & 0 & -\frac{\sqrt{3}}{\sqrt{2}} & 0 \\ 0 & \frac{1}{\sqrt{2}} & 0 & -\frac{\sqrt{3}}{\sqrt{2}} & -\frac{1}{2} & 0 \\ -\frac{\sqrt{3}}{\sqrt{2}} & 0 & \frac{1}{\sqrt{2}} & 0 & 0 & \frac{1}{2} \end{pmatrix},$$

$$D_{4x} = \begin{pmatrix} 0 & 0 & 0 & -\frac{3}{2} & 0 & 0 \\ 0 & 0 & \frac{1}{2} & 0 & 0 & -\frac{1}{\sqrt{2}} \\ 0 & \frac{1}{2} & 0 & 0 & \frac{1}{\sqrt{2}} & 0 \\ -\frac{3}{2} & 0 & 0 & 0 & 0 & 0 \\ 0 & 0 & \frac{1}{\sqrt{2}} & 0 & 0 & -1 \\ 0 & -\frac{1}{\sqrt{2}} & 0 & 0 & -1 & 0 \end{pmatrix},$$

$$D_{4y} = \begin{pmatrix} 0 & -\frac{\sqrt{3}i}{2} & 0 & 0 & \frac{\sqrt{3}i}{2\sqrt{2}} & 0 \\ \frac{\sqrt{3}i}{2} & 0 & i & 0 & 0 & -\frac{i}{2\sqrt{2}} \\ 0 & -i & 0 & -\frac{\sqrt{3}i}{2} & -\frac{i}{2\sqrt{2}} & 0 \\ 0 & 0 & \frac{\sqrt{3}i}{2} & 0 & 0 & \frac{\sqrt{3}i}{2\sqrt{2}} \\ -\frac{\sqrt{3}i}{2\sqrt{2}} & 0 & \frac{i}{2\sqrt{2}} & 0 & 0 & i \\ 0 & \frac{i}{2\sqrt{2}} & 0 & -\frac{\sqrt{3}i}{2\sqrt{2}} & -i & 0 \end{pmatrix},$$

$$D_{4z} = \begin{pmatrix} 0 & 0 & \frac{\sqrt{3}}{2} & 0 & 0 & \frac{\sqrt{3}}{2\sqrt{2}} \\ 0 & 1 & 0 & -\frac{\sqrt{3}}{2} & \frac{1}{2\sqrt{2}} & 0 \\ \frac{\sqrt{3}}{2} & 0 & -1 & 0 & 0 & \frac{1}{2\sqrt{2}} \\ 0 & -\frac{\sqrt{3}}{2} & 0 & 0 & \frac{\sqrt{3}}{2\sqrt{2}} & 0 \\ 0 & \frac{1}{2\sqrt{2}} & 0 & \frac{\sqrt{3}}{2\sqrt{2}} & -1 & 0 \\ \frac{\sqrt{3}}{2\sqrt{2}} & 0 & \frac{1}{2\sqrt{2}} & 0 & 0 & 1 \end{pmatrix}. \quad [7]$$

The fitted parameters are shown in Table S1, and the fitted band structures along $M-\Gamma-R$ high-symmetry lines are shown in Fig. S8 (b).

By using the band structure in Fig. S8 (a) and (b), the calculated conductivity with a 12 meV broadening is shown in Fig. S9.

E_0 (meV)	ϵ (meV)	λ_1 (eV Å)	λ_2 (eV Å)	λ_3 (eV Å)	λ_4 (eV Å)
43.7	18.4	0.7904	-0.0052	-0.0222	0.0219

Table S1. The fitted parameters of the tight-binding model with SOC

Appendix G: Four-band tight-binding model

Following Ref. (5), we have constructed a four-band tight-binding model for CoSi that is consistent with its crystal symmetry to describe the closest four energy bands to the Fermi level of this material. In general, this model can describe any material in space group 198, and without spin-orbit coupling it is defined through three material-dependent parameters: v_1, v_p, and v_2. In addition to these paramaters (5) we incorporate the orbital embedding as described in Appendix F of Ref. (6). The orbital embedding x describes the position (or embedding) of orbitals in real space. It enters as a momentum-dependent unitary transformation (7), leaving the band structure unaltered, but modifying its eigenfunctions and, as a result, the predicted optical conductivity.

To describe CoSi specifically, we fix $x_{\mathrm{CoSi}} = 0.3865$, as determined by crystallographic databases, and find v_1, v_p, and v_2 by fitting the tight-binding spectrum to the DFT bands. To capture the separation in energy between the multi-fold nodes at Γ and R, we fix it to match that found by DFT, which equals 210 meV. By expanding the Hamiltonian to linear order in momentum around Γ and R, we see that the parameter v_p sets the Fermi velocity of the three-fold and double Weyl fermion at the Γ and R points to $v_F^\Gamma = v_p/2$ and $v_R^\Gamma = v_p/(2\sqrt{3})$, respectively (8). To set the right energy scale in the tight-binding model we add a constant energy shift of $E_0 = 0.551$ eV, $H = H_{198}(v_1, v_p, v_2; x) + (E_0 - \mu)\mathbb{I}_{4\times4}$. All chemical potentials are measured with respect to this energy shift.

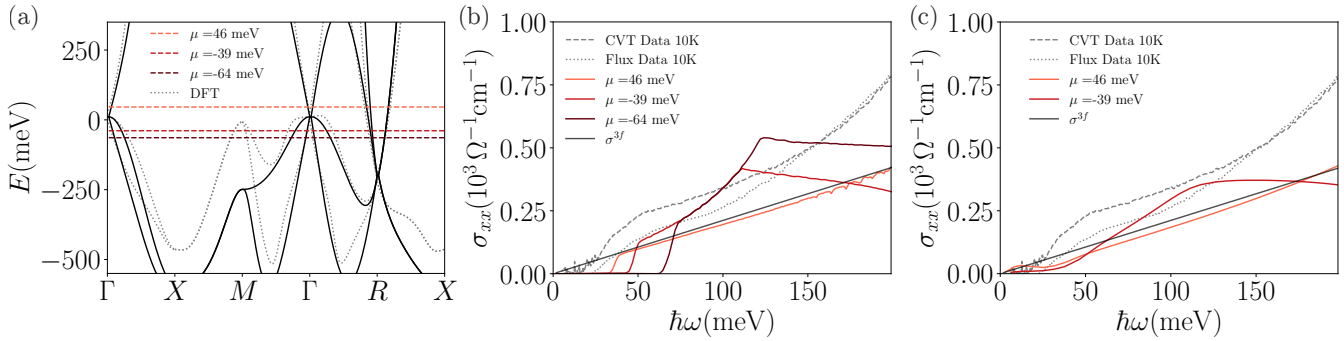

Fig. S10. (a) Band structure of CoSi obtained using a four-band tight-binding model with $v_1 = 1.29$, $v_2 = 0.25$ and $v_p = 0.55$ compared to DFT bands (dotted grey). Fermi levels for different chemical potentials are marked as horizontal dashed lines. (b) Optical conductivity for the chemical potentials shown in (a) with 0 meV broadening. For reference we show as a solid line the optical conductivity of a threefold fermion $\sigma^{3f} = \frac{\omega}{3\pi v_F}$ with $v_F = v_p/2$. (c) Optical conductivity at two fixed chemical potentials, one above and one below the Γ node, calculated with a finite broadening of 12 meV.

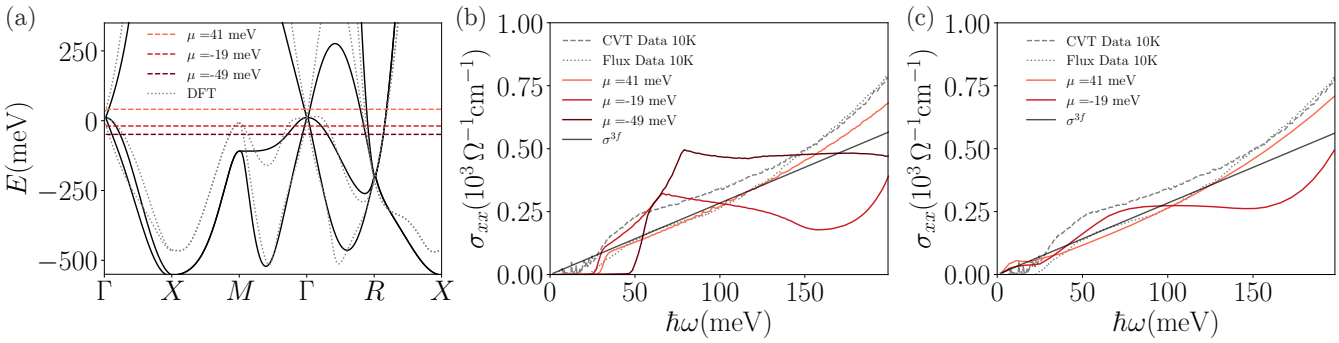

Fig. S11. Same as Fig. S10 with $v_p = 0.41$. (a) Band structure of CoSi obtained using a four-band tight-binding model with $v_1 = 1.29$, $v_2 = 0.25$ and $v_p = 0.41$ compared to DFT bands (dotted grey). Fermi levels for different chemical potentials are marked as horizontal dashed lines. (b) Optical conductivity at the chemical potentials in (a). For reference, we show as a solid line the optical conductivity of a threefold fermion $\sigma^{3f} = \frac{\omega}{3\pi v_F}$ with $v_F = v_p/2$. (c) Optical conductivity at two fixed chemical potentials, one above and one below the Γ node calculated with a finite broadening of 12 meV.

It is illustrative then to compare two different fits, one that matches well the Fermi velocity near the Γ point, and a second one to match the Fermi velocity at the R point. For $v_p = 0.55$, we fit the Fermi velocity of the bands near the Γ point (see Fig. S10 (a)). Upon closer inspection, we find that it provides a better description of the upper band of the three-fold crossing at the Γ point than that of the middle and lower bands. For $v_p = 0.41$, we fit to the Fermi velocity of the bands near the R point (see Fig. S11 (a)). Despite being a good fit for the R point, we observe this to be a fair description also of the lower and middle bands at the Γ point away from the Γ node. For both fits, we obtain $v_1 = 1.29$ and $v_2 = 0.25$ for the remaining tight-binding parameters.

In Fig. S10 and Fig. S11 (b) we compare the optical conductivities obtained for different chemical potentials crossing the node with 0 meV broadening. The (c) panels show the optical conductivity for selected chemical potentials and with a finite phenomenological Lorentzian disorder broadening of 12 meV. For both values of v_p, we find that a chemical potential that crosses the bands below the Γ node results in a peak and dip structure. In the case of $v_p = 0.55$, which amounts to $v_F = 1.23$ eV·Å, the conductivity has an increasing trend when lowering the chemical potential, which agrees well with the trend observed in Fig. S12 in Appendix H. The curve with $v_p = 0.55$, $\mu = -39$ meV shown in Fig. S10(c) falls closest to the Wannier tight-binding calculation.

It is interesting to note that although a good agreement between the four-band tight-binding model and the flux sample data is found for $v_p = 0.41$ with the chemical potential above the node, and a 12 meV broadening (Fig. S11 (c)), this value of the chemical potential does not agree with the rest of our observations. As discussed at length in this appendix and in the main text, from transport results to ab-initio calculations we find that CoSi is a compensated semimetal with a hole pocket at the Γ, implying that the chemical potential in the sample is below the node. In this case, the curve with $\mu = -39$ meV $v_p = 0.55$ in Fig. S10 (c) results in the best fit to the data and first-principles calculations.

Appendix H: The effect of chemical potential on the calculated conductivity in the Wannier tight-binding models

The chemical potential in real materials could be different from that obtained in DFT, due to extrinsic effects such as the presence of impurities. Therefore, we have calculated the optical conductivity with different chemical potentials. The conductivity calculated without SOC coupling is shown in Fig. S12. Under the condition that the chosen chemical potential is lower than the flat middle band near the Γ point, transitions will always occur between the lower band and the middle band when the energy of the incoming photon is small (< 0.1 eV), and occur near the R point when the energy is relatively large (> 0.2 eV). Therefore, changing the chemical potential will influence the position and the shape of the dip structure ($\sigma_1(\omega \approx 0.25$ eV)) in two ways. Firstly, as the chemical potential decreases, more transitions could occur between the lower band and the middle band, and this would lead to an increase in conductivity at the downward part of the dip structure. Secondly, more transitions could also occur near the R point due to the decrease in chemical potential, so it is also expected that the upward region of the dip structure will increase. Combining these two results, decreasing the Fermi level will tend to flatten (and perhaps eventually remove) the dip structure.

When turning on SOC, the conductivity calculated with different chemical potentials are shown in Fig. S12. The conclusions drawn from the non-SOC case can also be applied here; namely, decreasing the chemical potential will smooth the dip structure. Furthermore, we studied the case where the chemical potential is placed between the middle band pair (the purple curve in Fig. S12 (c)). In this case, the number of transitions between the lower band pair and the middle band pair is reduced, which leads to a decrease in the lower-frequency region. However, the transitions which occur near the R point are almost unaffected, which justifies the fact that the slope of the upward part of the dip structure is similar to that of the intrinsic Fermi level.

To summarize, assuming a lower chemical potential increases the conductivity below 0.2 eV, but still the agreement with the CVT-grown sample is not as good as the agreement achieved for the flux-grown sample. This is an indication that either the additional contribution in the CVT-grown (001) sample is not coming from inter-band transition or the origin of defects in the CVT sample is slightly different. Another possible scenario is the additional contribution from surface states in the (001) facets (9), which is absent in the (111) facets.

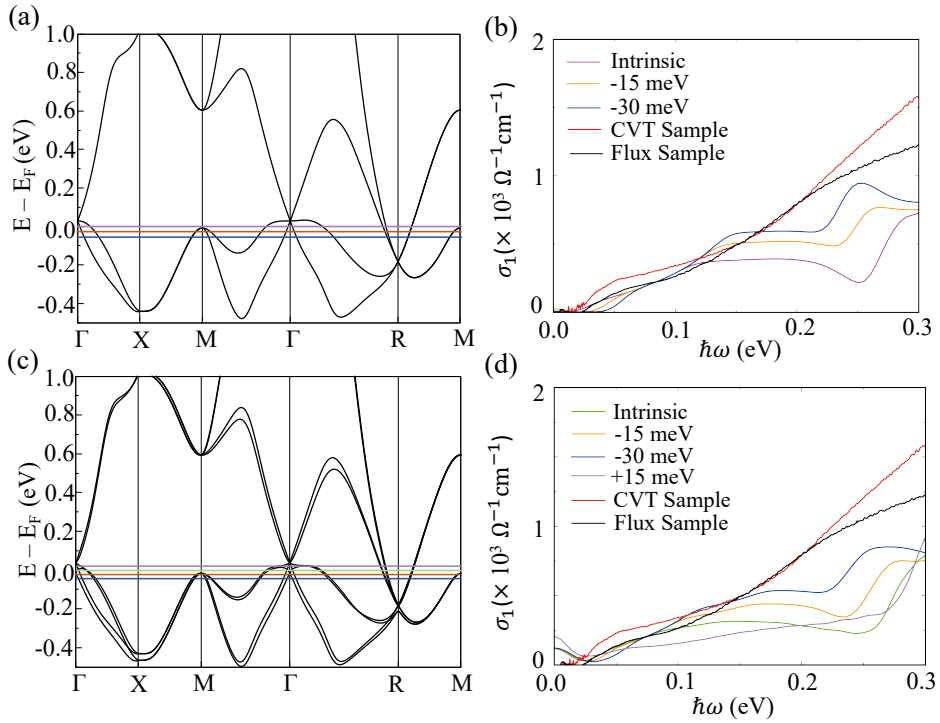

Fig. S12. (a) The position of several chosen chemical potentials superimposed on the calculated band structure without SOC. (b) The optical conductivity calculated with each of the chosen chemical potentials. (c, d) Same as (a, b), but incorporating SOC.

References

1. CC Homes, M Reedyk, DA Cradles, T Timusk, Technique for measuring the reflectance of irregular, submillimeter-sized samples. *Appl. Opt.* **32**, 2976–2983 (1993).
2. M Dressel, G Grüner, *Electrodynamics of Solids.* (Cambridge University press), (2002).
3. D van der Marel, A Damascelli, K Schulte, A Menovsky, Spin, charge, and bonding in transition metal mono-silicides. *Phys. B: Condens. Matter* **244**, 138 – 147 (1998) Proceedings of the International Conference on Low Energy Electrodynamics in Solids.
4. FP Mena, et al., Suppressed reflectivity due to spin-controlled localization in a magnetic semiconductor. *Phys. Rev. B* **73**, 085205 (2006).
5. G Chang, et al., Unconventional chiral fermions and large topological fermi arcs in rhsi. *Phys. review letters* **119**, 206401 (2017).
6. MÁ Sánchez-Martínez, F de Juan, AG Grushin, Linear optical conductivity of chiral multifold fermions. *Phys. Rev. B* **99**, 155145 (2019).
7. F Flicker, et al., Chiral optical response of multifold fermions. *Phys. Rev. B* **98** (2018).
8. JL Manes, Existence of bulk chiral fermions and crystal symmetry. *Phys. Rev. B* **85** (2012).
9. G Chang, et al., Unconventional photocurrents from surface fermi arcs in topological chiral semimetals. *Phys. Rev. Lett.* **124**, 166404 (2020).